

LA-UR-18-28802 (Accepted Manuscript)

## Influence of morphology on the blinking mechanisms and the excitonic fine structure of single colloidal nanoplatelets

Hu, Zhongjian  
Singh, Ajay  
Goupalov, Serguei V.  
Hollingsworth, Jennifer Ann  
Htoon, Han

Provided by the author(s) and the Los Alamos National Laboratory (2019-04-01).

**To be published in:** Nanoscale

**DOI to publisher's version:** 10.1039/C8NR06234J

**Permalink to record:** <http://permalink.lanl.gov/object/view?what=info:lanl-repo/lareport/LA-UR-18-28802>

**Disclaimer:**

Los Alamos National Laboratory, an affirmative action/equal opportunity employer, is operated by Triad National Security, LLC for the National Nuclear Security Administration of U.S. Department of Energy under contract 89233218CNA00001. By approving this article, the publisher recognizes that the U.S. Government retains nonexclusive, royalty-free license to publish or reproduce the published form of this contribution, or to allow others to do so, for U.S. Government purposes. Los Alamos National Laboratory requests that the publisher identify this article as work performed under the auspices of the U.S. Department of Energy. Los Alamos National Laboratory strongly supports academic freedom and a researcher's right to publish; as an institution, however, the Laboratory does not endorse the viewpoint of a publication or guarantee its technical correctness.

# Influence of Morphology on Blinking Mechanisms and Excitonic Fine Structure of Single Colloidal Nanoplatelets

Zhongjian Hu<sup>1,†</sup>, Ajay Singh<sup>1,†</sup>, Serguei V. Goupalov<sup>2,3</sup>, Jennifer A. Hollingsworth<sup>1</sup>  
& Han Htoon<sup>1,\*</sup>

<sup>1</sup>Center for Integrated Nanotechnologies, Material Physics and Applications Division  
Los Alamos National Laboratory, Los Alamos, NM 87545

<sup>2</sup>Department of Physics, Jackson State University, Jackson, MS 39217

<sup>3</sup>Ioffe Institute, St. Petersburg 194021, Russia

<sup>†</sup>Equal contribution

\*Correspondence and requests for materials should be addressed to H.H.

(email: [htoon@lanl.gov](mailto:htoon@lanl.gov))

Electronic supplementary information (ESI) available.

## Abstract

Colloidal semiconductor nanoplatelets with electronic structure as quantum wells have recently emerged as exciting materials for optoelectronic applications. Here we investigate how morphology affects important photoluminescence properties of single CdSe and core/shell CdSe/CdZnS nanoplatelets. By analyzing photoluminescence intensity-lifetime correlation and second-order photon correlation results, we demonstrate that, irrespective of morphology, Auger recombination plays only a minor role in dictating the blinking behavior of the nanoplatelets. We find that a rough shell induces additional nonradiative channels presumably related to defects or traps of an imperfect shell. Furthermore, polarization-resolved spectroscopy analysis reveals exciton fine-structure splitting on the order of several tens of meV in rough-shell nanoplatelets at room temperature, which is attributed to exciton localization and substantiated with theoretical calculations taking into account the nanoplatelet shape and electron-hole exchange interaction.

## 1. Introduction

Colloidal semiconductor nanocrystals (NCs) have been attracting considerable interest in both fundamental and applied scientific research in the past two decades.<sup>1-3</sup> Compared with the extensively studied 0D quantum dots (QDs) and 1D nanorods/nanowires, only in the past several years have colloidal 2D nanoplatelets (NPLs) with controllable morphology and dimensions been introduced.<sup>4-9</sup> The NPLs usually have a lateral dimension larger than the bulk exciton Bohr radius and a thickness of several monolayers (MLs), thus representing free-standing quasi 2D quantum wells. With the thickness that is well-defined and can be engineered with atomic precision, the NPLs have narrow photoluminescence (PL) linewidths at room temperature not affected by inhomogeneous broadening.<sup>7, 10-12</sup> Meanwhile, 2D NPLs typically have a giant oscillator strength and a fast recombination of band-edge excitons.<sup>10, 12-15</sup> In addition, interesting directed PL emission perpendicular to the platelet has recently been demonstrated in

CdSe NPLs.<sup>16</sup> These remarkable and unique photophysical properties have made the colloidal NPLs very attractive for a broad range of applications such as lasing and light emitting diodes.<sup>17-22</sup>

PL blinking (i.e., intensity intermittency), a phenomenon that has been extensively studied in colloidal QDs, has also been reported for single NPLs.<sup>12, 23, 24</sup> Several studies have attributed the blinking of single NPLs to Auger recombination.<sup>12, 24</sup> On the other hand, for 2D quantum wells having a strong electronic confinement mainly in one dimension, there is a theoretically stringent momentum conservation rule for Auger recombination.<sup>18</sup> In fact, suppressed Auger recombination in NPLs has been demonstrated in multiple works recently.<sup>18, 25, 26</sup> Such contradictory reports warrant further investigations regarding the Auger recombination and its role in PL blinking behavior in NPLs. In addition, 2D NPLs have a large surface area. Therefore, shell growth on core NPLs and shell morphology are expected to have a strong impact on the excited state photophysics and PL spectral properties. Although some fundamental PL properties of core/shell (C/S) NPL structures have been reported by several studies,<sup>23, 27, 28</sup> up to now morphological effects on PL blinking behavior (in connection with its relation to Auger recombination), exciton fine-structure, and PL polarization have not been investigated.

Herein, we study in detail impacts of CdZnS shell growth and shell morphology—smooth or rough—on PL properties of single CdSe NPLs in terms of PL blinking, Auger recombination, biexciton quantum yield, polarization, and exciton fine-structure. Specifically, we demonstrate that, irrespective of shell growth and morphology, Auger recombination plays only a minor role in defining blinking behavior of single NPLs. We further report polarization-resolved spectral measurements which reveal exciton fine-structure splitting in the presence of a rough shell, which is attributed to exciton localization.

## **2. Results and Discussion**

### **2.1 Morphological and bulk optical characterizations**

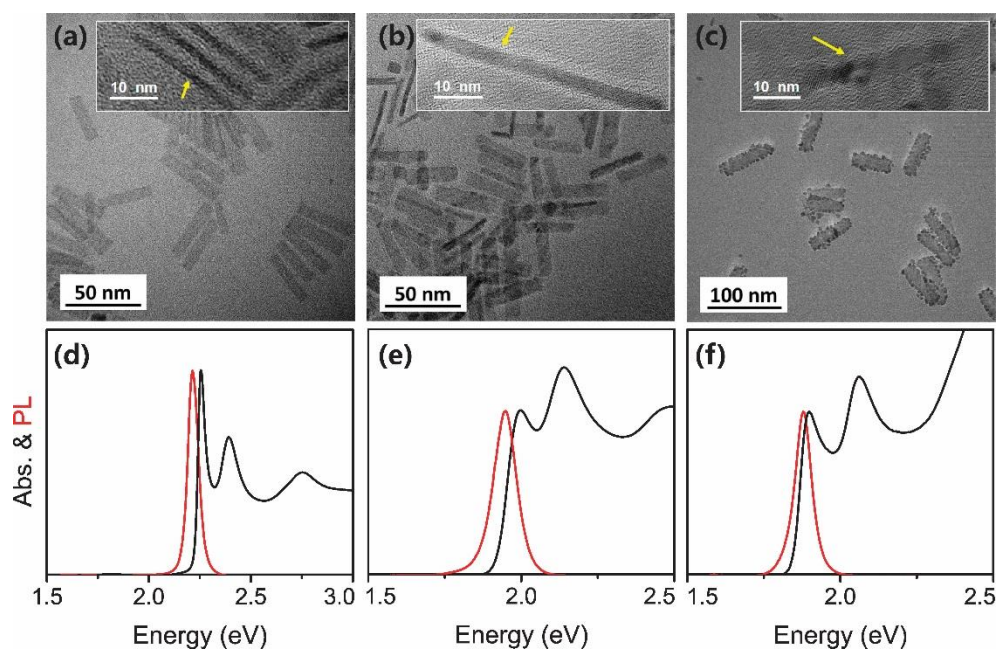


**Fig. 1** Transmission electron microscopy (TEM) images of core CdSe NPLs (a), CdSe NPLs with smooth CdZnS shell (b), and CdSe NPLs with rough CdZnS shell (c). The insets in (a-c) display TEM images of NPLs standing on their edges. Yellow arrows in the insets denote edge-on NPLs. Note that the vertically oriented NPLs in most cases can only be seen in concentrated samples. The bottom panels (d-f) show the absorption (black) and PL (red) spectra of solutions for the core NPLs, the smooth-shell NPLs, and the rough-shell NPLs, respectively.

The CdSe NPLs were synthesized following previously reported method.<sup>10</sup> CdZnS shell were added to the core CdSe NPLs using modifications of two literature methods, i.e., layer-by-layer growth<sup>23</sup> and one-pot continuous shell growth<sup>28</sup>, resulting in C/S NPLs with smooth and rough shell morphology, respectively (see Experimental Section and Supporting Information). Fig. 1(a-c) displays TEM images for the core CdSe NPLs, the smooth CdZnS shell NPLs, and the rough-shell NPLs, respectively. The core NPLs have a lateral dimension of  $\sim 7 \pm 1$  nm in width and  $\sim 50 \pm 7$  nm in length. In consideration of these lateral dimensions and the bulk Bohr radius of 5.6 nm of CdSe, there is no confinement along the length and slight confinement along the width.<sup>12, 29</sup> The thickness of core NPLs is  $\sim 1.5$  nm, based on analysis of core NPLs standing on their edges (inset of Fig. 1a), which corresponds to 5 monolayers of CdSe. This thickness also fits in the relationship between thickness and the absorption excitonic peak.<sup>27</sup> For both the smooth- and rough-shell NPLs (Fig. 1b-c), the lateral dimensions remain similar to those of the NPL

core, suggesting that shell growth occurred mainly on the top and bottom sides. The smooth-shell NPLs lying flat on the TEM substrate exhibit uniform contrast (Fig. 1b). TEM imaging for edge-on NPLs (inset of Fig. 1b) reveals that the smooth-shell NPLs are covered by a shell with uniform thickness of  $\sim 1$  nm. As shown in Fig. 1c, the rough-shell NPLs exhibit significant contrast variation. The particle-like species on rough-shell NPL surfaces and edges are CdZnS grains within the rough CdZnS shell, which are formed during the quick one-pot synthesis.<sup>28</sup> TEM imaging for edge-on rough-shell NPLs (inset of Fig. 1c) clearly shows that the thickness of rough-shell NPLs fluctuates in a range of 3-5 nm, suggesting the 1.5 nm-thick core is covered by a non-uniform shell.

Absorption and PL spectra of NPLs suspended in hexanes/chloroform solutions are shown in Fig. 1(d-f). For the core NPLs, two absorption peaks are observed at 2.28 eV and 2.41 eV that correspond to the heavy- and light-hole excitons, respectively (Fig. 1d). Emission peaks at 2.24 eV with a full-width-at-half-maximum (FWHM) of 48 meV and a PL quantum yield (QY) of 15-20%. The absorption and emission spectral results are consistent with the previously reported data for 5-monolayer CdSe NPLs.<sup>12, 27</sup> CdZnS shell growth induces strong red shifts in both absorption and emission, which can be attributed to the electronic wavefunction extension from the CdSe core into the shell material.<sup>23</sup> The smooth-shell NPLs and the rough-shell NPLs have emission peaks at 1.93 eV (PL QY: 60-65%) and 1.87 eV (PL QY: 45-50%), respectively (Fig. 1e, 1f). The difference in the emission maximum between the smooth- and rough-shell NPLs is likely due to the rough shell being slightly thicker, or to the observed thickness fluctuations. In addition, compared to the core NPLs, the C/S NPLs have broader and similar emission linewidths:  $\sim 60$  meV and  $\sim 57$  meV for the smooth- and rough-shell NPLs, respectively. The increased linewidth in C/S NPLs can be attributed to the extension of electron-phonon coupling into the shell material and the high phonon energy of the shell material.<sup>23, 26</sup>

## 2.2 Blinking of single nanoplatelets

PL intensity blinking (i.e., intermittency) is a ubiquitous phenomenon observed in individual semiconductor nanocrystals.<sup>30</sup> The blinking behaviors have also been observed for NPLs.<sup>12, 23</sup> Analogous to the cases of the C/S heterostructures of QDs, the growth of shell greatly reduces PL blinking. This is reflected in the time traces of fluorescence intensity shown in Fig. 2(a-c): the C/S NPLs exhibit a much longer “on” time compared with the core NPLs. Such an improvement is further demonstrated in a statistical photostability analysis of the on-time fraction of  $\sim 50$  NPLs under one-hour continuous excitation. It reveals that the on-time fraction increases from  $\sim 4\%$  for the core NPLs to  $\sim 31\%$  for the smooth-shell NPLs and  $\sim 42\%$  for the rough-shell NPLs (Supporting Information Fig. S1). The higher on-time fraction value of the rough-shell NPLs relative to the smooth-shell NPLs could be related to the generally thicker shell of the former.

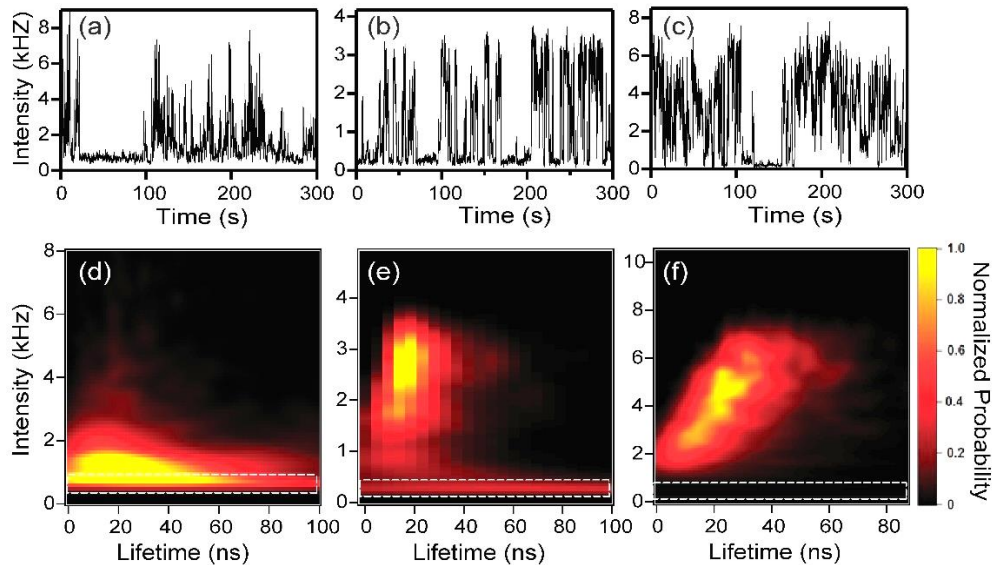


**Fig. 2** Representative PL intensity time traces of the core CdSe NPLs (a), the smooth-shell CdSe/CdZnS NPLs (b), and the rough-shell CdSe/CdZnS NPLs (c). Panel (d-f) display the FLID diagrams for the corresponding time traces (a-c) for three types of NPLs, respectively. For the color scale in the FLID diagrams, yellow represents the most frequent probability of lifetime-intensity pair, and probabilities less than 1% of this maximum are indicated by black. A linear scaling is used between the yellow and black. The white dashed box in (d-e) indicates the signal from the background. It should be noted that the rather widely distributed lifetimes for intensity levels below  $\sim 2$  kHz in Figure 2d and  $\sim 1$  kHz in Figure 2e should not be considered for correlation between intensity and lifetime. This is because these intensity levels are too close to the noise level and therefore the fitting results of lifetimes are not reliable.

The phenomenon of PL blinking, since its first report by Nirmal et al in single QDs, has been intensively studied in terms of the fundamental mechanisms.<sup>30, 31</sup> Although the deterministic mechanism of PL blinking is still under debate, the widely-accepted explanation of the off-state (or the grey state that weakly fluoresces) is that the nonradiative Auger recombination as a result of photo-induced charging is responsible. To understand the in-depth mechanism of the blinking behavior in NPLs, we perform detailed analysis for about twenty single NPLs of each type of NPL: we analyze the PL lifetimes for photons collected at different intensity levels and correlate PL intensities and lifetimes in fluorescence lifetime-intensity distribution (FLID) 2D diagrams (see Experimental Section).<sup>32</sup> Single NPLs of the same type exhibit similar correlation trends between intensity and lifetime in FLID diagrams. It should also be noted that PL decay dynamics of CdSe nanoplatelets are usually multiexponential.<sup>22, 33</sup> In the present work, the PL decays are typically fitted to three-exponential function and the lifetime exhibited in the FLID diagrams is fraction-weighted average lifetime,  $\langle \tau \rangle = \sum a_i \tau_i^2 / \sum a_i \tau_i$ , where  $a_i$  is amplitude and  $\tau_i$  is lifetime. Fig. 2(d-f) displays the FLID diagrams for PL intensity time traces shown in Fig. 2(a-c), respectively (see Fig. S2 for more set of data). For the core NPL and the smooth-shell NPL, FLID contour maps (Fig. 2d and 2e) show that the PL count rates distribute vertically while the PL lifetimes nearly keep constant. This observation is confirmed further by similar PL decays extracted for different PL intensity ranges shown in Supporting Information Fig. S3. The behavior of PL intensity fluctuation with no correlated change in lifetime excludes Auger recombination and other nonradiative processes that lead to the loss of carrier population from the emissive state as dominant mechanisms because such processes will always lead to reduced lifetimes. This result rather points to a situation that fluctuation of exciton population arriving to the emissive state is dominating the blinking process. Under excitation at a constant power, such population fluctuation could only arise from variation in light absorption cross-section or ultrafast nonradiative recombination of photo-excited carriers before they have a chance to relax to the lowest emissive state. Because there is no reason to expect the absorption cross-section to fluctuate with

time, here we tentatively attribute the latter process as the mechanism for the PL intensity fluctuation. Nearly identical PL intensity-independent lifetime behavior was observed in CdSe/CdS and InP/CdS colloidal QDs as well as InGaAs epitaxial QDs and attributed to a similar mechanism.<sup>32, 34, 35</sup> For NPLs studied in the present work, the wavefunctions of photoexcited hot carriers of the core can leak out to the shell significantly as a result of thin shell. This could result in carrier interactions with the surface/defect states and then ultrafast nonradiative recombination capable of competing with relaxation to the lowest emissive state, therefore leading to the PL intensity-independent lifetime behavior. On the other hand, while our experiment provides the evidence that such an ultrafast process is dominating the blinking behavior, we cannot fully exclude the nonradiative decay of emissive exciton state. The intensity-lifetime correlated fluctuation that could arise from such process could simply be masked by the dominant PL intensity-independent lifetime behavior. In fact, the broad distribution of lifetimes in Fig. 2d and 2e as well as multi-exponential decay clearly visible in Fig. S3 indicates the existence of such processes.

By contrast, for the rough-shell NPLs, PL lifetime varies along with PL intensity as shown in Fig. 2c and 2f. Such a blinking phenomenon is referred to as A-type blinking in our previous work<sup>32</sup> and rationalized by nonradiative Auger recombination. Here the recombination of charged excitons results in the off-state, wherein the recombining electron-hole pair transfers its energy to the third charge nearby, while the recombination of neutral band edge excitons leads to the PL emission of on-state. Some previous studies have tentatively attributed the blinking behavior observed for NPLs to Auger recombination mechanism.<sup>12, 24</sup> However, there also have been several reports showing that Auger process in NPLs is greatly hampered.<sup>18, 25, 26, 36, 37</sup> These contradictory reports surrounding Auger recombination warrant an in-depth investigation regarding its role in the blinking behavior of NPLs.

### **2.3 Auger recombination and biexciton**

Auger recombination is closely related to the biexciton in nanocrystals. According to the statistical scaling, the biexciton Auger decay rate can be expressed as twice the sum of Auger decay rate of negative

trion and positive trion, i.e.,  $k_{A,BX} = 2(k_{A,X^-} + k_{A,X^+})$ .<sup>38-40</sup> Even when this relation is not strictly valid, the biexciton Auger decay rate should still reflect an upper limit of the trion Auger process. As the QY of biexciton and charged excitons ( $QY_{BX}$  and  $QY_{TX}$ , respectively) scales inversely with their Auger decay rates,  $QY_{BX}$  should provide a lower bound of the  $QY_{TX}$  that define the intensity of the dark state in A-Type blinking mechanism. Next, we perform the second-order photon correlation,  $g^{(2)}$ , analysis to measure  $QY_{BX}$  relative to single exciton QY ( $QY_{SX}$ ) and inferred the lower limit of  $QY_{TX}$ . For typical  $g^{(2)}$  traces obtained with pulsed laser excitation, the area ratio between the center peak (delay time at 0) to the side peaks,  $R$ , signifies the emission nature of the emitters. An  $R$  value of 0, i.e., photon antibunching, is characteristic of single quantum emitters, while a non-zero  $R$  value indicates either emitter clustering or biexciton emission.

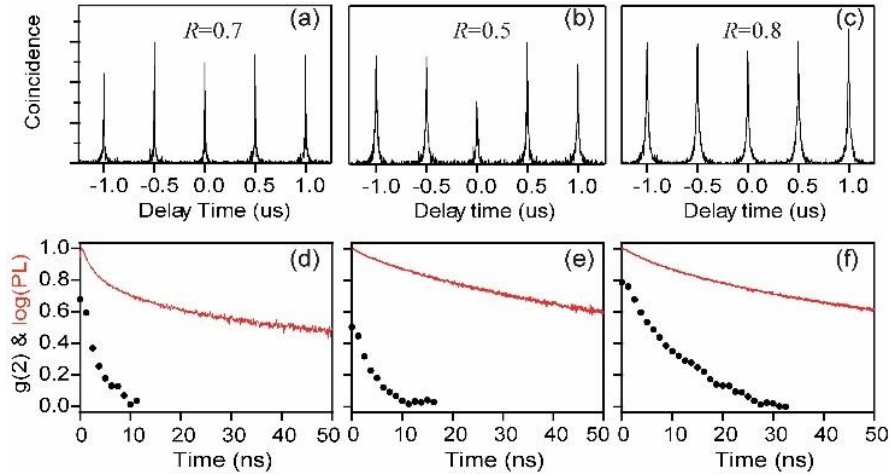


**Fig. 3** Photon correlation data of the core CdSe NPL (a), the smooth-shell NPL (b), and the rough-shell NPL (c). The corresponding PL decays (red) and the decays of  $R$  value as a function of gated time (black dotted) are shown in (d-f). These data were obtained from the same respective NPLs demonstrated in Fig. 2.

Fig. 3(a-c) demonstrates  $g^{(2)}$  plots and corresponding  $R$  values, as insets, in each panel for the same three NPLs, for which the blinking traces are shown in Fig. 2. One can see that all three types of NPLs exhibit high  $R$  values above 0.5. To disentangle the effects of NPLs clustering and biexciton emission,

we employ the time-gated antibunching technique developed previously.<sup>41,42</sup> In this software-based time gating approach, the contribution of the possible faster biexciton emission can be reduced (removed) by applying a time-gate that is approaching (longer than) the lifetime of biexcitons. Therefore, a quick decay of the  $R$  value to zero with the gated delay time signifies that the  $R$  value is contributed by the biexciton emission of a single NPL. Fig. 3(d-f) displays decays of the  $R$  value as functions of the applied gated delay time for the three NPLs. One can see that the  $R$  value drops much faster than the overall fluorescence, which is shown as a red curve for comparison, for all three types of NPLs. The fast decay of  $R$  towards 0 within a gated delay time less than 10-30 ns suggests that the initial  $R$  values above 0.5 are caused by high  $QY_{BX}$  in the NPLs rather than NPLs clustering. For isolated nanocrystals,  $R$  is directly proportional to the ratio of  $QY_{BX}$  to  $QY_{SX}$ , that is,  $R = g^{(2)}(0)/g^{(2)}(t) = QY_{BX}/QY_{SX}$ .<sup>43, 44</sup> Our analysis of  $R$  for about twenty NPLs for each type reveals average values of  $0.63 \pm 0.28$ ,  $0.61 \pm 0.14$ ,  $0.78 \pm 0.14$  for the core NPLs, the smooth-shell NPLs, and the rough-shell NPLs, respectively. These data are consistent with the recent results reported by Ma et al.<sup>24</sup> Considering the high  $QY_{BX}/QY_{SX}$  values and that  $QY_{BX}$  gives the lower bound of the  $QY_{TX}$  that defines the intensity of the dark state, we can conclude that charged excitons cannot be responsible for blinking behavior in the rough NPLs. We therefore attribute the faster decay of lower intensity levels observed in Fig. 2f to some nonradiative channels that are related to imperfect shell morphology, such as surface defects, traps, etc. This result is consistent with the observations made on ensembles of CdSe/CdS NPLs by Kunneman et al, who reported hole trapping at a defect site basing on transient absorption and terahertz conductivity measurements.<sup>25</sup> In addition, a close look at the ratios of PL intensity levels and their corresponding lifetimes reveals that the intensity drops faster than the PL lifetime. For instance, as shown in Supporting Information Fig. S3c and S3f, the ratio between the highest to the lowest highlighted intensity bands is  $\sim 4.3$ , while the ratio between their corresponding lifetimes is only  $\sim 2.3$ . This observation indicates that, besides the nonradiative processes related to rough morphology, the loss of photoexcited carrier before the relaxation to the emission state

also contributes to the blinking of rough-shell NPLs. Our results regarding the blinking of NPLs not only provide a detailed understanding of the blinking mechanism and its relation with morphology but indicate possible routes to making non-blinking NPLs by structure engineering. For instance, a thicker smooth shell is desirable, as it would reduce both the number of surface defects/traps and the hot-carrier tunneling probability.

## 2.4 Polarization anisotropy and polarization-resolved PL spectra

Polarization characteristics of NCs convey information on the nature of exciton transition dipole and fine structure.<sup>45-47</sup> We first investigate the polarization anisotropy of total PL emission by splitting PL image into two orthogonal polarizations (i.e., horizontally/vertically polarized emission  $I_H/I_V$ ) using a Wollaston prism.<sup>46, 47</sup> The polarization is modulated by rotating a half-wave plate in front of the prism. Fig. 4a demonstrates the normalized horizontal emission,  $I_{NH}$  ( $I_{NH}=I_H/(I_H+I_V)$ ), as a function of the emission angle. A fit with a sine-squared function to the data gives the degree of polarization,  $P=(I_{NH,max}-I_{NH,min})/(I_{NH,max}+I_{NH,min})$ . The core NPLs exhibit high degree of polarization with P values of  $0.68\pm 0.20$ . The NPLs with shell, irrespective of the shell morphology, exhibit lower degrees of polarization with P values of  $0.44\pm 0.11$ ,  $0.42\pm 0.13$  for the smooth and the rough-shell NPLs, respectively (Supporting Information Fig. S4). Since the dominant majority of NPLs lie flat on the substrate (i.e.,  $x$ - $y$  plane perpendicular to the detection direction) as shown in Fig. 1a-c, the observed polarization originates from dipoles in the  $x$ - $y$  plane of NPLs.

It has been previously shown that symmetry breaking in semiconductor nanocrystals can result in fine structure splitting of the bright exciton, leading to two states linearly and orthogonally polarized along the nonequivalent semiminor axes of the nanocrystals.<sup>47-50</sup> To examine exciton fine structure in NPLs, we acquire the polarization-resolved PL spectra of individual NPLs by spectrally dispersing the

two orthogonal PL channels after the Wollaston prism using imaging spectrometer.<sup>46, 47</sup> With this detection scheme, horizontal- (H) and vertical-polarized (V) PL spectral components from individual NPLs are observed as pairs of spectra in the upper and lower regions of the CCD camera. Fig. 4b-4d displays representative orthogonally-polarized PL emission spectra (black and red curves) as a function of emission detection angle for a core NPL, a smooth-shell NPL, and a rough-shell NPL, respectively, at room temperature. The polarization-resolved PL spectra of the core NPLs exhibit high degree of linear polarization with no spectral splitting between two orthogonally polarized PL spectra. Surprisingly, polarization-resolved PL spectra of ~66% of the rough-shell NPLs (Fig. 4d) and ~45% of smooth-shell NPLs exhibit three energetically distinct, linearly polarized emissive states with energy splitting of ~25 meV. Out of these three states, the highest and lowest energy states have almost identical polarization orientation whereas the polarization of the middle state exhibits phase shift relative to that of the highest and lowest energy states. The remainder of the smooth-shell (~55%, Fig. 4c) and rough-shell NPLs (~34%) show broad PL spectra, without an obvious three-peak-splitting feature and with low degree of linear polarization consistent with total PL polarization anisotropy (Fig. 4a).

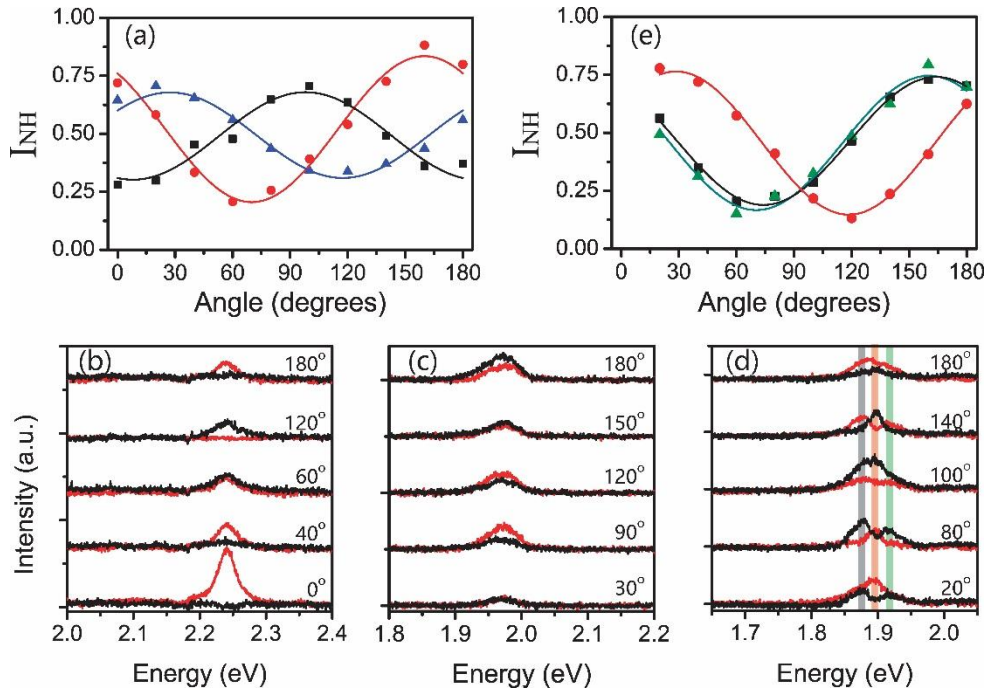


**Fig. 4 (a)** Typical polarization modulations obtained from imaging as a function of emission collection angle for single NPLs: the core NPLs (red), the smooth-shell NPLs (black), and the rough-shell NPLs (blue), respectively. The solid lines are fits to the data. **(b-d)** Room-temperature polarization-resolved spectra collected at different emission detection angles (shown as inset) for a single core NPL **(b)**, a single smooth-shell NPL **(c)**, and a single rough-shell NPL **(d)**, respectively. Red and black curves correspond to horizontal- (H) and vertical-polarized (V) spectral components. **(e)** The polarization modulations measured for the three highlighted 2-nm-wide wavelength bands in panel **(d)** shown with the same color. The solid lines are fits to the data.

Recent studies of relatively symmetric NPLs reported observation of polarization behavior consistent with a 2 D planar dipole corresponding to the heavy-hole exciton radiative doublet.<sup>16, 51</sup> Because our NPLs are highly asymmetric with the width and length of  $\sim 7$  nm and  $\sim 50$  nm, respectively, we expect the emissive exciton state to be split into two states. The thermalized excitons mainly occupy the low energy state of the two which dominates the emission with linear transition dipole oriented along the long axis of the NPL. While this picture can explain strongly linearly polarized emission of the core only NPLs, it cannot explain the emergence of the three emissive states in cases of the smooth- and rough-shell NPLs. Because the three emissive states were observed more frequently in rough-shell NPLs, we hypothesize that the localization of excitons in confinement potential minima resulting from the thickness fluctuations of NPLs is responsible. That is, the emitting states are not at thermal equilibrium. Populations of the emitting states are subject of rate equations implying efficient phonon-assisted transitions between the emitting states. To test this hypothesis, we construct a theoretical model of a NPL that localizes an exciton in a region of the width  $2L_y=70$  Å in the  $y$ -direction and varying localization length along the  $x$ -direction ( $2L_x$ ), which has the size of the surface roughness (Fig. 5a). For such a NPL, we expect four states, with two orthonormal states each for delocalized exciton ( $E_{3x}$  &  $E_{4y}$ ) and localized exciton ( $E_{1x}$  &  $E_{2y}$ ), respectively (Fig. 5a). To estimate energy splitting between these states, we use the well-known expression for the exciton resonance frequency renormalization due to the long-range electron-hole exchange interaction,  $\delta\omega_0^{(\alpha)}$ , for excitons localized in quantum wells<sup>52, 53</sup> (the index  $\alpha$  indicates the polarization of the exciton sublevels) and assume that the envelope wave function of an exciton

localized on the roughness has a Gaussian form.<sup>53</sup> Detailed description of theoretical calculations can be found in Supporting Information Note 3. Since the NPLs sizes are less than the emission wavelength, the final exchange-induced splitting can be expressed as

$$\delta\omega_0^{(y)} - \delta\omega_0^{(x)} \approx -\frac{\omega_{LT}a_B^3L_xL_y}{2\pi\tilde{a}^2} \int_0^\infty dt t^2 \int_0^{2\pi} d\varphi \cos 2\varphi e^{-t^2 \cos^2 \varphi L_x^2/2} e^{-t^2 \sin^2 \varphi L_y^2/2} \\ \times \int dz \Phi(z) \int dz' \Phi(z') e^{-t|z-z'|}$$

where,  $\omega_{LT}$  and  $a_B$  are the longitudinal-transverse splitting and the Bohr radius of a free exciton in the bulk material, respectively,  $\tilde{a}$  is the effective two-dimensional Bohr radius,  $\Phi(z)=\varphi_{e1}(z)\varphi_{hh1}(z)$  is the product of the electron and hole envelope wave functions along the axis of the quantum well or NPL (here we use the envelope wave functions for carriers confined in a quantum well with infinitely high barriers). For our estimate we will take  $\hbar\omega_{LT}=0.95$  meV,<sup>54</sup>  $a_B=56$  Å. Nanoplatelet excitons are known to have the effective two-dimensional Bohr radius  $< 10$  Å,<sup>55</sup> for an estimate we take  $\tilde{a}=7$  Å. The resulting dependence of the anisotropic exchange splitting on the size of the localizing potential along  $x$ ,  $L_x$ , at the fixed size along  $y$ ,  $L_y=35$  Å, is shown in Fig. 5b. The splitting is zero for  $L_x=L_y$ . Comparing the observed splitting with this dependence one can estimate the size of the localizing potential as  $2L_x$ . Our calculation yields a splitting between two delocalized exciton states  $E_{4y}-E_{3x}$  to be 63.5 meV as the delocalized exciton corresponds to the limit  $L_x \rightarrow \infty$  (in particular,  $L_x > 200$  Å). Because this splitting is larger than the thermal energy at room temperature, we can assume that the highest energy state  $E_{4y}$  is not accessible to the exciton population and therefore leading to the appearance of three peaks. Localization of exciton in  $\sim 100$  Å region (i.e.,  $L_x \sim 50$  Å) gives rise to  $E_{2y}-E_{1x}$  splitting of  $\sim 25$  meV, as observed in our experiments.  $E_{1x}$  and  $E_{3x}$  are linearly polarized along the long axis of the NPLs and  $E_{2y}$  is polarized in the perpendicular direction. This corresponds to our observation that the two side peaks have essentially the same polarization orientation. It is also noteworthy that at low temperature we did not observe polarization-resolved

fine structure splitting in these C/S NPLs (Fig. S5). We attribute such an observation to the unpopulated upper states at low temperature.

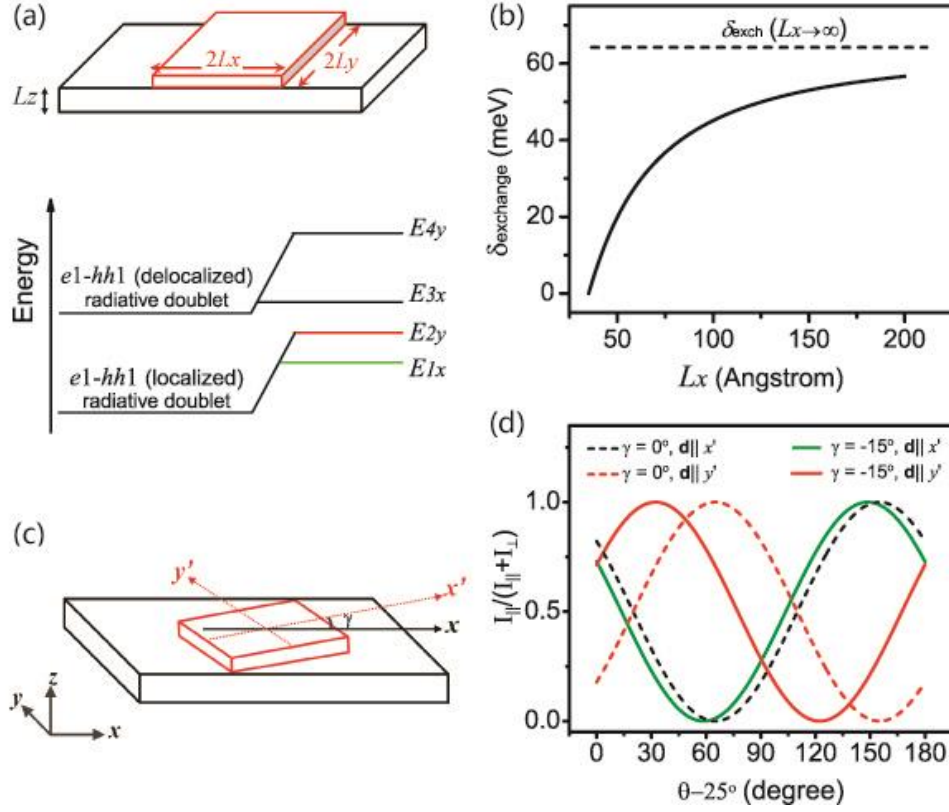


**Fig. 5** (a) Top: A schematic of a NPL with a width of  $2L_y$  and a thickness of  $L_z$  (black box). The theoretical modeling assumes that the exciton is localized on the red box, which has a width of  $2L_y$ , a length of  $2L_x$ , and a thickness equivalent to the surface roughness. Bottom: Fine structural scheme of energy levels of the exciton radiative doublets for both delocalized and localized excitons before and after electron-hole exchange interaction is taken into account, respectively. (b) Dependence of the anisotropic exchange splitting,  $\hbar(\delta\omega_0^{(y)} - \delta\omega_0^{(x)})$ , on the localization size along  $x$ ,  $L_x$ . The localization size along  $y$ -axis is fixed:  $2L_y = 70 \text{ \AA}$ . (c) A possible orientation of the exciton localization region that can result in a polarization “nonorthogonality”. (d) Angular dependencies of  $I_{\parallel}^{x'}(\theta)/(I_{\parallel}^{x'} + I_{\perp}^{x'})$  and  $I_{\parallel}^{y'}(\theta)/(I_{\parallel}^{y'} + I_{\perp}^{y'})$  (i.e., polarization modulation of emission dipole along the  $x'$  and  $y'$  axis, respectively) for  $\gamma = 0^\circ$  and  $\gamma = -15^\circ$ .  $\theta$  represents the angle between the  $x$ -axis and the “horizontal” polarization of the analyzer.

While the middle peak in the above theoretical picture should be polarized normal to the two side peaks, our result shown shows that the polarization of the middle peak usually has a phase shift in a range of 50-90°. For example, a ~55° phase shift is observed in Fig. 4e. This inconsistency could result from a misalignment of the orientation of the exciton localization region (due to surface roughness fluctuation) with respect to the main axes of the NPL (Fig. 5c, also refer to Supporting Information Note 3 for details). To illustrate this point, we construct a model as displayed in Fig. 5c, for which we assume that the main axes of the exciton localization region ( $x', y'$ ) form a small angle  $\gamma$  with respect to the main axes of the NPL ( $x, y$ ). A drastic difference in high-frequency dielectric constants between the NPLs ( $\epsilon_{in} \sim 6$ ) and the ambient air ( $\epsilon_{out} \sim 1$ ) leads to a strong depolarization field in the  $y$ -direction perpendicular to the axis of the NPL elongation. As a result of misalignment, the dipole oriented along  $y'$  has a small projection onto  $x$  axis (Fig. 5c). But, since the electric field along  $y$  axis is suppressed due to the depolarization effect, the electric field of light, emitted by the dipole polarized along  $y'$ , has comparable components along  $x$  and  $y$ . Similarly, the dipole oriented along  $x'$  has a small projection onto  $y$  axis. But the depolarization effect leads to the fact that the corresponding small component of the electric field in the emitted light is further suppressed. As a result, the depolarization effect strongly affects polarization of the light emitted by the dipole polarized along  $y'$  and has almost no effect on polarization of the light emitted by the dipole polarized along  $x'$ . Our detailed calculation (see Supporting Information Note 3) reveals that a misalignment angle of  $\gamma \sim 15^\circ$  can approximately reproduce the large phase shift in the polarized PL intensity from  $y'$  polarized dipole and the negligible shift in the polarized PL intensity from  $x'$  polarized dipole (Fig. 5d) as we observed in Fig. 5e. Taken together, the theoretical results are in excellent agreement with our experimental observations. Finally, we want to mention that the orientation of localized states on individual NPLs are different between NPLs. In addition, there are ~55% smooth-shell NPLs and ~34% rough-shell NPLs which do not show polarization-resolved fine structure. As a result, the overall

ensemble averaging effect could wash out such polarization-resolved fine structure when measured at ensemble scale even for orientated monolayers.

### 3. Conclusion

We have systematically investigated the morphological effects on PL properties of CdSe/CdZnS NPLs. The deposition of CdZnS shell on core CdSe NPLs not only reduces PL blinking of single NPLs but, more importantly, results in variations in the optical and electronic properties depending on shell morphology. We demonstrated that, regardless of shell growth and morphology, Auger recombination can only play a minor role in PL blinking of single NPLs. The deposition of a rough CdZnS shell leads to opening of additional nonradiative channels compared to smooth-shell NPLs, which are possibly due to the existence of trap or defect sites in an imperfect shell. Polarization-resolved spectral analysis revealed exciton fine-structure splitting on the order of tens of meV at room temperature in the majority of rough-shell NPLs. We showed that exciton can get localized at a surface irregularity resulting from the rough shell morphology. Both the fine-structure splitting and PL polarization resulting from exciton localization are sensitive to the size and shape of the exciton localization region. The PL polarization is further affected by the depolarization effect determined by the shape of NPL. These conclusions are supported by theoretical calculations which are in excellent agreement with experimental observations.

### Experimental Section

*Nanoplatelets Synthesis.* CdSe core NPLs were synthesized according to previously published procedure with slight modifications.<sup>10</sup> Smooth CdZnS shell on CdSe core NPLs were synthesized following atomic layer deposition approach with some modification.<sup>23</sup> To achieve rough CdZnS shell, we used previously published continuous shell growth protocol with minor modification.<sup>28</sup> The extra ligands in the nanoplatelets solutions were removed using ethanol for precipitation and re-dispersing in hexane or chloroform. Details about the materials and synthesis of NPLs are available in Supporting Information Note 1.

*Single NPLs spectroscopy.* Single NPLs samples were prepared by drop-casting suspensions of NPLs in hexanes onto clean glass coverslips. Single NPLs spectroscopy experiments were carried out on a typical laser scanning confocal optical microscope using a pulsed 403 nm diode laser (2 MHz,  $\sim 70$  ps pulse width). PL emission from individual NPLs was collected with a 100 $\times$ , 0.85 NA objective lens and cleaned with long pass filters. The pump condition is: power:  $\leq 6$  nW; repetition rate: 2 MHz; excitation wavelength: 405 nm. Based on the literature,<sup>24, 56</sup> it is estimated that the exciton density  $\langle N \rangle$  (i.e., photons absorbed per pulse) is no higher than 0.4 for the NPLs measured. Time-resolved PL and  $g^{(2)}$  experiments were performed with two single photon avalanche photodiodes (SPAD, SPCM-AQR-14, PerkinElmer) placed in a Hanbury-Brown-Twiss geometry and connected to a Hydraharp 400 TCSPC system (time channels is 65,536) operating in a time-tag time-resolved mode. The temporal time resolution is  $\sim 500$  ps. To generate the FLIDs, we accumulated at least 500,000 counts (typically,  $10^6$  counts if the single dots are photon stable enough). Single NPLs PL spectra were measured by directing PL emission to a spectrograph (SP-2300i, Princeton Instruments) and imaged with a CCD camera. Emission polarization anisotropy and polarization-resolved PL experiments were performed in a wide-field mode. Herein, the 403 nm diode laser was focused to a spot size with diameter of  $\sim 60$   $\mu\text{m}$  and was used to excite the samples. The PL images and spectra were collected with the same spectrometer and CCD camera as used in the confocal mode. A Wollaston prism was used to spatially split the emission into its respective horizontal and vertical locations along the spectrometer slit. This enabled a simultaneous measurement of two orthogonal components. A half-wave plate was deployed in front of the Wollaston prism to tune the emission angle.

## **Conflict of Interest**

The authors declare no conflict of interest.

## **Acknowledgments**

This work was performed, in part, at the Center for Integrated Nanotechnologies, an Office of Science User Facility operated for the U.S. Department of Energy (DOE) Office of Science, as part of CINT User Project 2017AU0142. Los Alamos National Laboratory (LANL), an affirmative action equal opportunity employer, is operated by Los Alamos National Security, LLC, for the National Nuclear Security Administration of the U.S. DOE under contract DE-AC52-06NA25396. Z.H., J.A.H. and H.H. were supported by LANL Laboratory Directed Research and Development Funds. A.S. was supported by a Los Alamos National Laboratory Director's Postdoctoral Fellowship. S.V.G. would like to thank M.O. Nestoklon and E.L. Ivchenko for useful discussions. The work of SVG was supported by the National Science Foundation (NSF-CREST Grant HRD-1547754).

## References

- 1 J. M. Pietryga, Y.-S. Park, J. Lim, A. F. Fidler, W. K. Bae, S. Brovelli and V. I. Klimov, *Chem. Rev.*, 2016, **116**, 10513-10622.
- 2 G. H. Carey, A. L. Abdelhady, Z. Ning, S. M. Thon, O. M. Bakr and E. H. Sargent, *Chem. Rev.*, 2015, **115**, 12732-12763.
- 3 F. Todescato, I. Fortunati, A. Minotto, R. Signorini, J. J. Jasieniak and R. Bozio, *Materials*, 2016, **9**, 672.
- 4 S. Ithurria and B. Dubertret, *J. Am. Chem. Soc.*, 2008, **130**, 16504-16505.
- 5 S. Ithurria, G. Bousquet and B. Dubertret, *J. Am. Chem. Soc.*, 2011, **133**, 3070-3077.
- 6 S. Ithurria and D. V. Talapin, *J. Am. Chem. Soc.*, 2012, **134**, 18585-18590.
- 7 E. Lhuillier, S. Pedetti, S. Ithurria, B. Nadal, H. Heuclin and B. Dubertret, *Acc. Chem. Res.*, 2015, **48**, 22-30.
- 8 M. Nasilowski, B. Mahler, E. Lhuillier, S. Ithurria and B. Dubertret, *Chem. Rev.*, 2016, **116**, 10934-10982.
- 9 A. C. Berends and C. de Mello Donega, *J. Phys. Chem. Lett.*, 2017, **8**, 4077-4090.
- 10 S. Ithurria, M. D. Tessier, B. Mahler, R. P. S. M. Lobo, B. Dubertret and A. L. Efros, *Nat. Mater.*, 2011, **10**, 936-941.
- 11 G. B. Griffin, S. Ithurria, D. S. Dolzhenkov, A. Linkin, D. V. Talapin and G. S. Engel, *J. Chem. Phys.*, 2013, **138**, 014705.
- 12 M. D. Tessier, C. Javaux, I. Maksimovic, V. Lorette and B. Dubertret, *Acs Nano*, 2012, **6**, 6751-6758.
- 13 L. Biadala, F. Liu, M. D. Tessier, D. R. Yakovlev, B. Dubertret and M. Bayer, *Nano. Lett.*, 2014, **14**, 1134-1139.
- 14 R. Scott, S. Kickhofel, O. Schoeps, A. Antanovich, A. Prudnikau, A. Chuvilin, U. Woggon, M. Artemyev and A. W. Achtstein, *Phys. Chem. Chem. Phys.*, 2016, **18**, 3197-3203.
- 15 A. W. Achtstein, A. Schliwa, A. Prudnikau, M. Hardzei, M. V. Artemyev, C. Thomsen and U. Woggon, *Nano. Lett.*, 2012, **12**, 3151-3157.
- 16 R. Scott, J. Heckmann, A. V. Prudnikau, A. Antanovich, A. Mikhailov, N. Owschimikow, M. Artemyev, J. I. Climente, U. Woggon, N. B. Grosse and A. W. Achtstein, *Nat. Nanotechnol.*, 2017, **12**, 1155.
- 17 Z. Chen, B. Nadal, B. Mahler, H. Aubin and B. Dubertret, *Adv. Funct. Mater.*, 2014, **24**, 295-302.
- 18 J. Q. Grim, S. Christodoulou, F. Di Stasio, R. Krahn, R. Cingolani, L. Manna and I. Moreels, *Nat. Nanotechnol.*, 2014, **9**, 891-895.
- 19 B. Guzelturk, Y. Kelestemur, M. Olutas, S. Delikanli and H. V. Demir, *Acs Nano*, 2014, **8**, 6599-6605.
- 20 M. Li, M. Zhi, H. Zhu, W.-Y. Wu, Q.-H. Xu, M. H. Jhon and Y. Chan, *Nat. Commun.*, 2015, **6**, 8513.
- 21 C. She, I. Fedin, D. S. Dolzhenkov, P. D. Dahlberg, G. S. Engel, R. D. Schaller and D. V. Talapin, *Acs Nano*, 2015, **9**, 9475-9485.
- 22 M. Olutas, B. Guzelturk, Y. Kelestemur, A. Yeltik, S. Delikanli and H. V. Demir, *Acs Nano*, 2015, **9**, 5041-5050.
- 23 M. D. Tessier, B. Mahler, B. Nadal, H. Heuclin, S. Pedetti and B. Dubertret, *Nano. Lett.*, 2013, **13**, 3321-3328.
- 24 X. Ma, B. T. Diroll, W. Cho, I. Fedin, R. D. Schaller, D. V. Talapin, S. K. Gray, G. P. Wiederrecht and D. J. Gosztola, *ACS Nano*, 2017, **11**, 9119-9127.
- 25 L. T. Kunneman, J. M. Schins, S. Pedetti, H. Heuclin, F. C. Grozema, A. J. Houtepen, B. Dubertret and L. D. A. Siebbeles, *Nano. Lett.*, 2014, **14**, 7039-7045.
- 26 L. T. Kunneman, M. D. Tessier, H. Heuclin, B. Dubertret, Y. V. Aulin, F. C. Grozema, J. M. Schins and L. D. A. Siebbeles, *J. Phys. Chem. Lett.*, 2013, **4**, 3574-3578.
- 27 M. D. Tessier, P. Spinicelli, D. Dupont, G. Patriarche, S. Ithurria and B. Dubertret, *Nano. Lett.*, 2014, **14**, 207-213.
- 28 B. Mahler, B. Nadal, C. Bouet, G. Patriarche and B. Dubertret, *J. Am. Chem. Soc.*, 2012, **134**, 18591-18598.
- 29 A. W. Achtstein, R. Scott, S. Kickhöfel, S. T. Jagsch, S. Christodoulou, G. H. V. Bertrand, A. V. Prudnikau, A. Antanovich, M. Artemyev, I. Moreels, A. Schliwa and U. Woggon, *Phys. Rev. Lett.*, 2016, **116**, 116802.
- 30 A. L. Efros and D. J. Nesbitt, *Nat. Nanotechnol.*, 2016, **11**, 661-671.
- 31 M. Nirmal, B. O. Dabbousi, M. G. Bawendi, J. J. Macklin, J. K. Trautman, T. D. Harris and L. E. Brus, *Nature*, 1996, **383**, 802-804.
- 32 C. Galland, Y. Ghosh, A. Steinbrueck, M. Sykora, J. A. Hollingsworth, V. I. Klimov and H. Htoon, *Nature*, 2011, **479**, 203-U275.
- 33 F. T. Rabouw, J. C. van der Bok, P. Spinicelli, B. Mahler, M. Nasilowski, S. Pedetti, B. Dubertret and D. Vanmaekelbergh, *Nano. Lett.*, 2016, **16**, 2047-2053.
- 34 B. D. Mangum, F. Wang, A. M. Dennis, Y. Gao, X. Ma, J. A. Hollingsworth and H. Htoon, *Small*, 2014, **10**, 2892-2901.
- 35 F. Hu, Z. Cao, C. Zhang, X. Wang and M. Xiao, *Scientific Reports*, 2015, **5**, 8898.
- 36 Q. Li and T. Lian, *Nano. Lett.*, 2017, **17**, 3152-3158.
- 37 M. Pelton, J. J. Andrews, I. Fedin, D. V. Talapin, H. Leng and S. K. O'Leary, *Nano. Lett.*, 2017, **17**, 6900-6906.
- 38 L.-W. Wang, M. Califano, A. Zunger and A. Franceschetti, *Phys. Rev. Lett.*, 2003, **91**, 056404.
- 39 P. P. Jha and P. Guyot-Sionnest, *ACS Nano*, 2009, **3**, 1011-1015.
- 40 Y.-S. Park, W. K. Bae, J. M. Pietryga and V. I. Klimov, *ACS Nano*, 2014, **8**, 7288-7296.
- 41 Z. Deutsch, O. Schwartz, R. Tenne, R. Popovitz-Biro and D. Oron, *Nano. Lett.*, 2012, **12**, 2948-2952.
- 42 B. D. Mangum, Y. Ghosh, J. A. Hollingsworth and H. Htoon, *Opt. Express*, 2013, **21**, 7419-7426.
- 43 G. Nair, J. Zhao and M. G. Bawendi, *Nano. Lett.*, 2011, **11**, 1136-1140.

- 44 Y. S. Park, A. V. Malko, J. Vela, Y. Chen, Y. Ghosh, F. Garcia-Santamaria, J. A. Hollingsworth, V. I. Klimov and H. Htoon, *Phys. Rev. Lett.*, 2011, **106**, 187401.
- 45 I. Chung, K. T. Shimizu and M. G. Bawendi, *P. Natl. Acad. Sci.*, 2003, **100**, 405-408.
- 46 H. Htoon, S. A. Crooker, M. Furis, S. Jeong, A. L. Efros and V. I. Klimov, *Phys. Rev. Lett.*, 2009, **102**, 017402.
- 47 H. Htoon, M. Furis, S. A. Crooker, S. Jeong and V. I. Klimov, *Phys. Rev. B*, 2008, **77**, 035328.
- 48 M. Furis, H. Htoon, M. A. Petruska, V. I. Klimov, T. Barrick and S. A. Crooker, *Phys. Rev. B*, 2006, **73**.
- 49 D. Gammon, E. S. Snow, B. V. Shanabrook, D. S. Katzer and D. Park, *Phys. Rev. Lett.*, 1996, **76**, 3005-3008.
- 50 M. Bayer, A. Kuther, A. Forchel, A. Gorbunov, V. B. Timofeev, F. Schäfer, J. P. Reithmaier, T. L. Reinecke and S. N. Walck, *Phys. Rev. Lett.*, 1999, **82**, 1748-1751.
- 51 F. Feng, T. L. N'Guyen, M. Nasilowski, C. M. Lethiec, B. Dubertret, L. Coolen and A. Maître, 2017.
- 52 S. V. Gupalov, E. L. Ivchenko and A. V. Kavokin, *J. Exp. Theor. Phys.*, 1998, **86**, 388-394.
- 53 S. V. Goupalov, E. L. Ivchenko and A. V. Kavokin, *Superlattice. Microst.*, 1998, **23**, 1205-1209.
- 54 V. A. Kiselev, B. S. Razbirin and I. N. Uraltsev, *Phys. Status. Solidi. B*, 1975, **72**, 161-172.
- 55 R. Benchamekh, N. A. Gippius, J. Even, M. O. Nestoklon, J. M. Jancu, S. Ithurria, B. Dubertret, A. L. Efros and P. Voisin, *Phys. Rev. B*, 2014, **89**, 035307.
- 56 J. Zhao, O. Chen, D. B. Strasfeld and M. G. Bawendi, *Nano. Lett.*, 2012, **12**, 4477-4483.